RESEARCH ARTICLE

Key Points:
- Coupling between magnetosphere and ionosphere resulting from the 2017 Memorial Day weekend geomagnetic storm
- Interactions between lower and upper atmosphere owing to tropospheric weather convection activity
- Equatorward and poleward traveling ionosperic disturbances (TIDs) over North America during quiet and disturbed periods

Correspondence to:
O. F. Jonah,
olujonah@mit.edu

TID Observations and Source Analysis During the 2017 Memorial Day Weekend Geomagnetic Storm Over North America

O. F. Jonah[1] (iD), A. Coster[1] (iD), S. Zhang[1] (iD), L. Goncharenko[1] (iD), P. J. Erickson[1] (iD), E. R. de Paula[2], and E. A. Kherani[2] (iD)

[1]Haystack Observatory, Massachusetts Institute of Technology, Westford, MA, USA, [2]National Institute for Space Research (INPE), São José dos Campos, Brazil

Abstract We investigate ionospheric perturbations associated with traveling ionospheric disturbance (TID) during the geomagnetic storm on Memorial Day weekend (28 May) 2017. Results show the presence of both equatorward propagating large-scale TIDs (LSTIDs) and poleward propagating medium-scale TIDs. Equatorward moving TIDs are connected with enhanced auroral activity owing to geomagnetic storm conditions, while poleward TIDs are believed to be induced by local atmospheric gravity wave sources originating from convection activities near the West Coast of North America. Measurements from magnetometers located in the west, central, and east regions of North America are used to evaluate energy inputs from the auroral belt, and these observations confirm that equatorward LSTIDs are due to geomagnetic disturbance. The observed LSTID waves were characterized by some uncommon features, such as horizontal wavefront stretching from coast to coast, aligned in the NW to SE direction, and propagating to the southwest (equatorward) direction during the storm main phase period. In contrast, during the recovery phase and on other experimental control days, the observed medium-scale TIDs were characterized with relatively smaller wavelengths aligned in the NW to SE direction and propagate primarily in the northeast (poleward) direction. Our results also reveal that LSTID waves appear to travel faster in the central continental region compared to LSTIDs in the western and eastern regions.

Plain Language Summary This study reveals the coupling of magnetosphere and ionosphere system as well as the interaction between the lower and upper atmosphere. Using the Global Navigation Satellite Systems (GNSS) receivers widely distributed over United States, networks of magnetometers over North America, and satellite measurements from the National Oceanic and Atmospheric Administration-Geostationary Operational Environmental Satellite (NOAA-GOES) and Sounding of the Atmosphere using Broadband Emission Radiometry (SABER) missions, we investigated the traveling ionospheric disturbance (TID) characteristics during the 28 May 2017 Memorial Day weekend geomagnetic storm and some quiet geomagnetic periods. Our results show equatorward large-scale TID owing to the 2017 Memorial Day weekend geomagnetic storm and poleward medium-scale TID propagation owning to atmospheric convection activity over the continental United States.

1. Introduction

The *F* region ionosphere plays host to numerous external forces that make it a highly variable medium. Traveling ionospheric disturbance (TID) is an example of the ionospheric wave whose activity level can be used to measure the state of ionosphere variability. Hence, the understanding of the characteristics of TIDs and their sources of generation are of enormous importance. The forces that cause TIDs have a variety of source regions, including from above (e.g., during space weather events), from below (e.g., during meteorological activities), and from those locally generated in the ionosphere. TIDs can generally be grouped into medium-scale TIDs (MSTIDs); with 100–300 m/s horizontal velocities, 200–500 km wavelengths, and 15-min to 1-hr wave periods and large-scale TIDs (LSTIDs) with 300–1,000 m/s horizontal velocities, 1,000–3,000 km wavelengths, and 1- to 2+-hr wave periods. MSTIDs occur more often than the large-scale ones (Tsugawa et al., 2003, 2004; Saito et al., 2002, 2007). MSTIDs generally have smaller velocities, periods, and wavelengths and are mainly seeded by sources from below such as atmospheric gravity waves (AGWs) from convective activities (Azeem et al., 2015; Jonah, 2017; Jonah et al., 2016), earthquakes, and seismic events

(Kherani et al., 2012). By contrast, LSTIDs have larger velocities, periods, and wavelengths and are generally triggered by heating related to auroral processes during geomagnetic storms (Chimonas & Hines, 1969; Ding et al., 2007). TID activity in the ionosphere can be significant in the transfer of energy and momentum from one region to another. Though TIDs have been investigated for more than four decades, they remain topic of active research and scientific debate. Oliver et al. (1997) developed a climatology of wave propagation based on 58 daytime incoherent scatter radar experiments at lower midlatitudes in Japan and tracked the passage of gravity wave-induced TIDs. The study showed that AGW-induced TIDs are ubiquitous in the ionosphere and can travel a long distance, with substantial variability during different times of day, seasons, and geomagnetic conditions. A remarkable AGW-TID study by Hines (1960) not only revealed that TIDs are mostly generated from AGWs, but this paper also presents the wave theory involved. Following this landmark research, there have been many AGW/TID studies ranging from medium to large scale with different characteristics observed. Hunsucker (1982) and Hocke and Schlegel (1996) provided comprehensive reviews of LSTIDs and MSTIDs. Horinouchi et al. (2002) used a cloud-resolving model to investigate mesoscale gravity wave generation mechanisms seeded by cumulus convection propagating from tropospheric altitudes to the mesosphere and lower thermosphere region. They reported a three-dimensional simulation of vertical propagation of mesoscale gravity waves, including interaction with other waves and wave breaking in the mesosphere and lower thermosphere regions. The wave breaking is another mechanism capable of generating secondary gravity waves with propagation to the upper atmosphere and subsequent TID creation at the ionospheric level, according to Vadas and Liu (2009). Jonah et al. (2016) studied tropospheric convection-induced AGWs and their ability to seed TIDs in the ionosphere during quiet geomagnetic conditions. According to Huba et al. (2015) and Duly et al. (2014), the electric field plays a principal role in the perturbation of density and neutral winds since $\nabla \cdot \mathbf{J}$ must be equal to zero (i.e., $\nabla \cdot \mathbf{J} = 0$) as a result of charge neutrality in the ionosphere. Furthermore, Jonah et al. (2017) conducted an experimental investigation of interhemispheric coupling, involving TID activity in the F region ionosphere and discussed the role of the electric field in the mapping of these TIDs from one hemisphere to another. Habarulema et al. (2016) showed that on a global scale, TIDs can transmit energy and momentum from one region to another during periods of geomagnetic disturbance.

The sources generating TIDs differ between daytime and nighttime, as do their characteristics. Using measurement results from Global Navigation Satellite System (GNSS) and ionograms, MacDougall et al. (2009) listed additional mechanisms through which AGWs can produce vertically propagating TIDs during the daytime. That study gave more weight to two prominent mechanisms: (1) the vertical component of motion due to AGW along inclined magnetic field lines and (2) the production of density variations by divergent motions of the AGW, which are also observed as height variations. In more recent studies, several varying velocities, wavelengths, and periods of TIDs have been identified by many authors. These properties of TIDs are mostly dependent on location or the magnitude of the sources that generate them. TIDs can also be generated by eclipses, representing one of the most spectacular sources of TID generation. The recent August 2017 total solar eclipse over the continental United States has been analyzed recently by different authors, including Coster et al. (2017) and Zhang et al. (2017). These studies show that besides the well-known density depletion during the eclipse, the sharp temperature gradient from the eclipse source can trigger the generation of AGW-induced TIDs of both large and medium scale in the ionosphere. Other previous northern hemisphere studies have examined the alignments and propagation directions of TIDs. In particular, works by Tsugawa et al. (2007), Kotake et al. (2007), and Otsuka et al. (2011, 2013) found that daytime TIDs were mainly in the northeast-southwest (NE-SW) direction with propagation in the southeast (equatorward) direction, whereas nighttime TIDs were aligned in the northwest-southeast (NW-SE) direction with propagation in the southwest (equatorward) direction. So far, there is no theory that correctly predicts these directivities. On the other hand, the Perkins instability theory predicts a correct wave vector $\mathbf{k}$ but different propagation direction and low growth rate (Kelley et al., 2011). However, very few studies of daytime TIDs over North America have shown TID alignments in the NW-SE direction with propagation in the northeast (poleward) direction. In fact, Ding et al. (2013) show that poleward traveling TIDs typically have smaller amplitudes and dissipate their energy faster as they travel poleward. Furthermore, Tsugawa et al. (2003) found that the damping rates of TIDs are mainly related to the ion-drag effect, which is proportional to ion-neutral collision frequency. Habarulema et al. (2015) indicated that during geomagnetic storm periods, charged particles could transfer momentum to neutral particles through collision (Lorentz forcing and Joule heating) resulting in internal

gravity waves (Richmond, 1978) that could in turn give rise to observed storm time TIDs. The modeling study by Horvath and Lovell (2010) showed that energy input from the auroral region can heat the thermosphere and propel an equatorward wind, providing a driving force for LSTIDs. We note as well that TIDs can have corresponding detrimental effects on radio wave propagation and space weather forecast (Hernandez-Pajares et al., 2006).

In the present study, we use a densely distributed Global Positioning System (GPS) receiver network over North America to investigate the impact of the 2017 Memorial Day weekend storm on the ionosphere. Our analysis reveals important characteristics of TIDs during both disturbed and quiet periods. Results of this study also include equatorward (poleward) propagations during nighttime (daytime), horizontal wavefront stretching from coast to coast, and different alignment of TID waves varying between daytime and nighttime. We used satellite observations to investigate possible source mechanism of poleward TIDs, and magnetometer measurements are employed to explore the storm time TID activity. Although the equatorward LSTIDs are seen only during the main phase of geomagnetic storm activity, poleward MSTIDs are present on all 3 days investigated (i.e., days 26–28 of May 2017) and propagate from the western region to eastern regions of North America. In section 2, we describe the estimation and background elimination methods used for TID detection. Sections 3–5 present analysed results discussion, and conclusions.

1.1. Data Description

Several different data sources were used for this study. GNSS geodetic receivers provide dense coverage over the continental United States, and after processing, data were obtained on total electron content (TEC) and differential TEC. Terrestrial magnetic field measurements were obtained from the array of AUTUMN and SuperMag magnetometer networks distributed over North America. The X and Y components of the magnetic field derived from the magnetometers were used to measure the fluctuation of electric current in the ionospheric system.

Cloud convection activity was obtained from the brightness temperature (BT) data provided by the National Aeronautics and Space Administration (NASA) Goddard Earth Sciences Data and Information Services Central (GES DISC). The data cover 60°S–60°N and 180°E–180°W, with 4-km pixel resolution. The BT data (equivalent blackbody temperatures) were obtained as an aggregated observation set merged from the European, Japanese, and U.S. geostationary satellites over the period of record (GOES-8/9/10/11/12/13/14/15/16, METEOSAT-5/7/8/9/10, and GMS-5/MTSat-1R/2/Himawari-8).

The Sounding of the Atmosphere using Broadband Emission Radiometry (SABER) experiment is an infrared multispectral radiometer, one of the four instruments aboard the NASA Thermosphere-Ionosphere-Mesosphere Energetics and Dynamics (TIMED) satellite. SABER data provided information for this study on the mesosphere and low thermosphere using a 10-channel broadband limb-scanning infrared radiometer with coverage ranging from 1.27 to 17 μm. SABER data determine altitude-resolved kinetic temperature, pressure, geopotential height, and other related parameters with altitude coverage of 10 to 110 km. The SABER version 2.0 data are used in the present study.

2. Method of TEC and TID Analysis

2.1. Method of TEC Bias and Error Estimation

The MIT Automated Processing of GPS (MAPGPS) software suite (Rideout & Coster, 2006) is used to calculate estimates of the TEC from the network of worldwide GPS receivers. These TEC estimates are output in 1° by 1° bins of latitude/longitude every 5 min distributed over those locations where data are available and are stored in Haystack's Madrigal database. Madrigal is an open source, web-based, distributed database system, which provides web-based data storage, retrieval, search, and visualization freely available to the space science community. Recently, the MAPGPS processing code was significantly enhanced to improve handling of errors. Errors are now tracked throughout the processing, and random and correlated errors are handled separately. This allows optimal estimation of binned measurements using weighted averages and allows error values to be calculated independently for each binned measurement. The bin-to-bin variability in the TEC measurements was greatly reduced using this approach. The current MIT Haystack receiver bais estimation procedure is based on the software described in Vierinen et al. (2016).
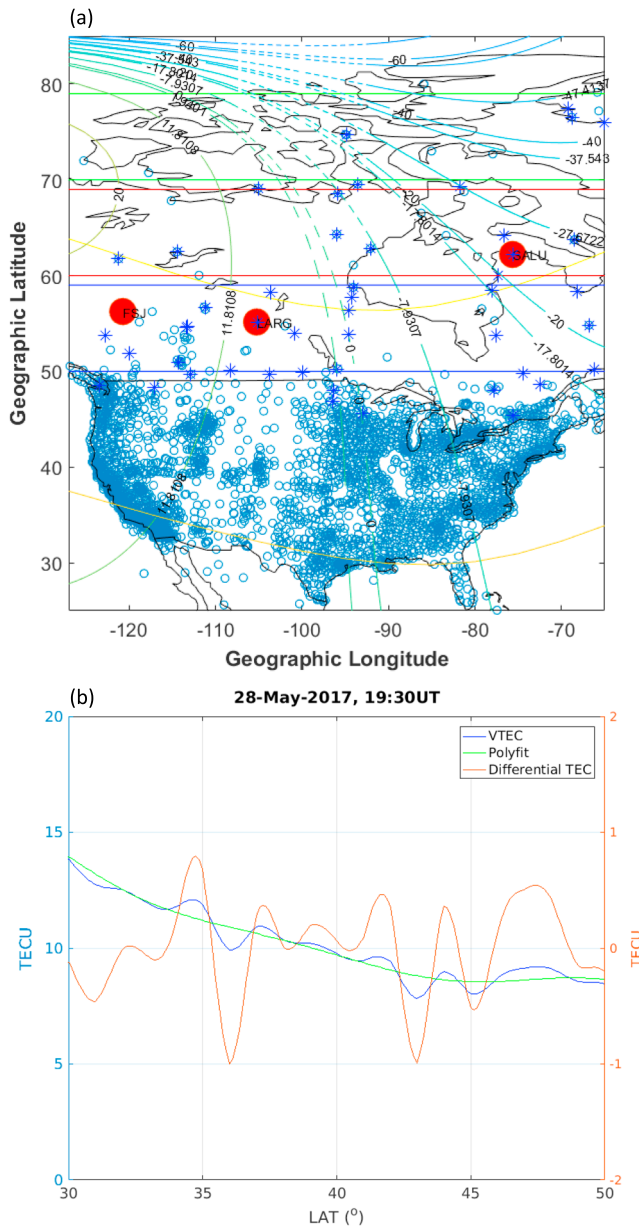
Figure 1. (a) The distribution of Global Navigation Satellite Systems (GNSS; blue circles), the distribution of magnetometer (red circles and blue stars), and the geomagnetic inclination and declination lines (yellow horizontal curves and green vertical curves, respectively). The blue, red, and green rectangular boxes represent 50–60 lat, 60–70° lat, and 70–80° lat, respectively. (b) Examples of traveling ionospheric disturbance analysis procedures at 115° longitude; the blue curve (to the left) represents observed vertical total electron content (VTEC), the green curve represents the polynomial fit for VTEC background, and the orange curve (to the right) represents differential TEC (ΔTEC).

2.2. Method of TID Analysis

Differential TEC is calculated from observed vertical TEC (VTEC) data by subtracting a polynomial fitter function derived from the VTEC data series during the period investigated according to equation (1):

$$\Delta VTEC = VTEC_t - VTEC_{t,\,fit}\,(x) \tag{1}$$

where x represents latitudinal variation, t represents the temporal variation, and $\Delta VTEC$ represents the differential VTEC. Longitudinal effects are not considered due to the weak nature of longitudinal variations of TEC in less than 10° longitude range (Ding et al., 2007). A step-by-step summary example of the differential VTEC determination process is shown in Figure 1b. The blue curve represents the VTEC, the green curve represents a chosen 10-order polynomial fit, and the resulting derived differential TEC is represented by the orange curve.

The order of the polynomial fit is tested by fitting the data with different polynomial orders and selecting the one with best fit for the data. The following goodness of fit tests are carried out:

First we compute the autocorrelation to determine the number of times sign changes in the fitter ΔTEC data using the expression:

$$(n-1)/2 - \sqrt{(n-1)} \leq q \leq (n-1)/2 + \sqrt{(n-1)},$$

where n in the number of data points in the time series and q is the number of times sign change occurs in the derived (*differential TEC*) time series.

Substituting n in the expression, we have $5.5 \leq q \leq 14.5$ for the interval, which is within the derived limit as represented in the example shown in Figure (1b). That is, the positive and negative signs alternate 10 times as shown in ΔTEC (orange curve) in Figure 1b.

A second goodness of fit test was applied by examining the coefficient of error determination using the r^2 regression model given by the equation:

$$r^2 = \frac{s_t + s_r}{s_t} \tag{2}$$

where $s_t = \sum\limits_{i=1}^{n}\left(TEC_i - \overline{TEC}\right)^2$ and $s_r = \sum\limits_{i=1}^{n}\left(TEC_i - \overline{fit}\right)^2$.

s_t is the amount of square deviation in the original TEC data (before taking the polynomial fit), while s_r is the amount of square deviation delta TEC (after taking the polynomial fit). The limit of r^2 should be between 0 and 1 (i.e., $0 \leq r^2 \leq 1$). Using the equations above, the r^2 for Figure 1b is 0.99, which is very close to 1 and represents a reasonable curve fitting and the best fit possible for the data series.

3. Results

3.1. The 2017 Memorial Day Weekend Geomagnetic Storm

Figure 2 summarizes geophysical and geomagnetic conditions prior to and during an intense geomagnetic storm of 27–28 May 2017, hereafter designated as the 2017 Memorial Day weekend storm. Figure 2 features from top to bottom a southward interplanetary magnetic field (Bz) below 20 nT for about 4 hr, with a minimum Dst of −120 nT at about 0820UT. The Kp index reached 7 during the main storm phase, with a strong increase in the AE from ~200 to ~1,300 nT that was also recorded. The coronal mass ejection that produced the 2017 Memorial Day weekend geomagnetic storm was generated on 23 May 2017 and hit the Earth's
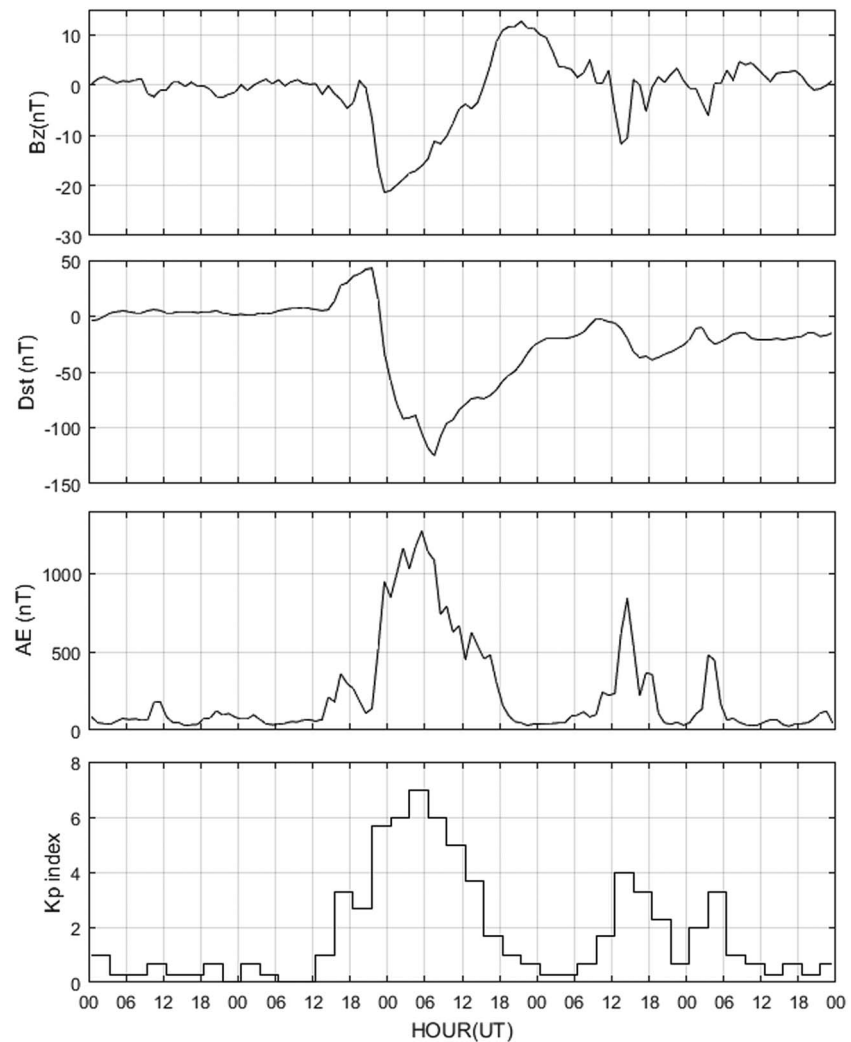
Figure 2. Geophysical and geomagnetic conditions during the 2017 Memorial Day weekend storm. From top to bottom: the Bz component of the magnetic field of interplanetary magnetic field, the Dst index, the AE index, and the Kp index for 26 to 30 May 2017.

magnetosphere on 27 May. Despite the slow solar wind speed, the composite magnetic field had a longer period of southward Bz turning, resulting in a strong G3 class geomagnetic storm. The area of effective impact was mainly poleward of 50°–55° geomagnetic latitude (as recorded by magnetometer stations around the region).

3.2. Equatorward and Poleward TIDs

For this study, a TID event is defined as a group of wavelike spatial and temporal structures traveling in the same region with similar directions. The TEC perturbations are defined as TIDs if they possess amplitudes greater than 0.2 TEC unit (Kotake et al., 2007), along with periods greater than 10 min and less than or equal to 3 hr (i.e., 10 min $<$ period $<$ 3 hr). The properties such as wavefront, wavelength, and period are determined from temporal variations in two-dimensional TID maps (e.g., Song et al., 2013) and keogram results. The horizontal velocity of the waves is calculated from basic wave relations (e.g., Jonah et al., 2016; Tsugawa et al., 2007).

Two main TID events were observed over North America during the 2017 Memorial Day weekend storm. (A) The first occurred during the main phase of the storm, between 0000 to 0830UT (1900–0330 eastern standard time). Figure 3 shows a time sequence of TIDs snapshots between 0045 and 0800UT (1945–0300
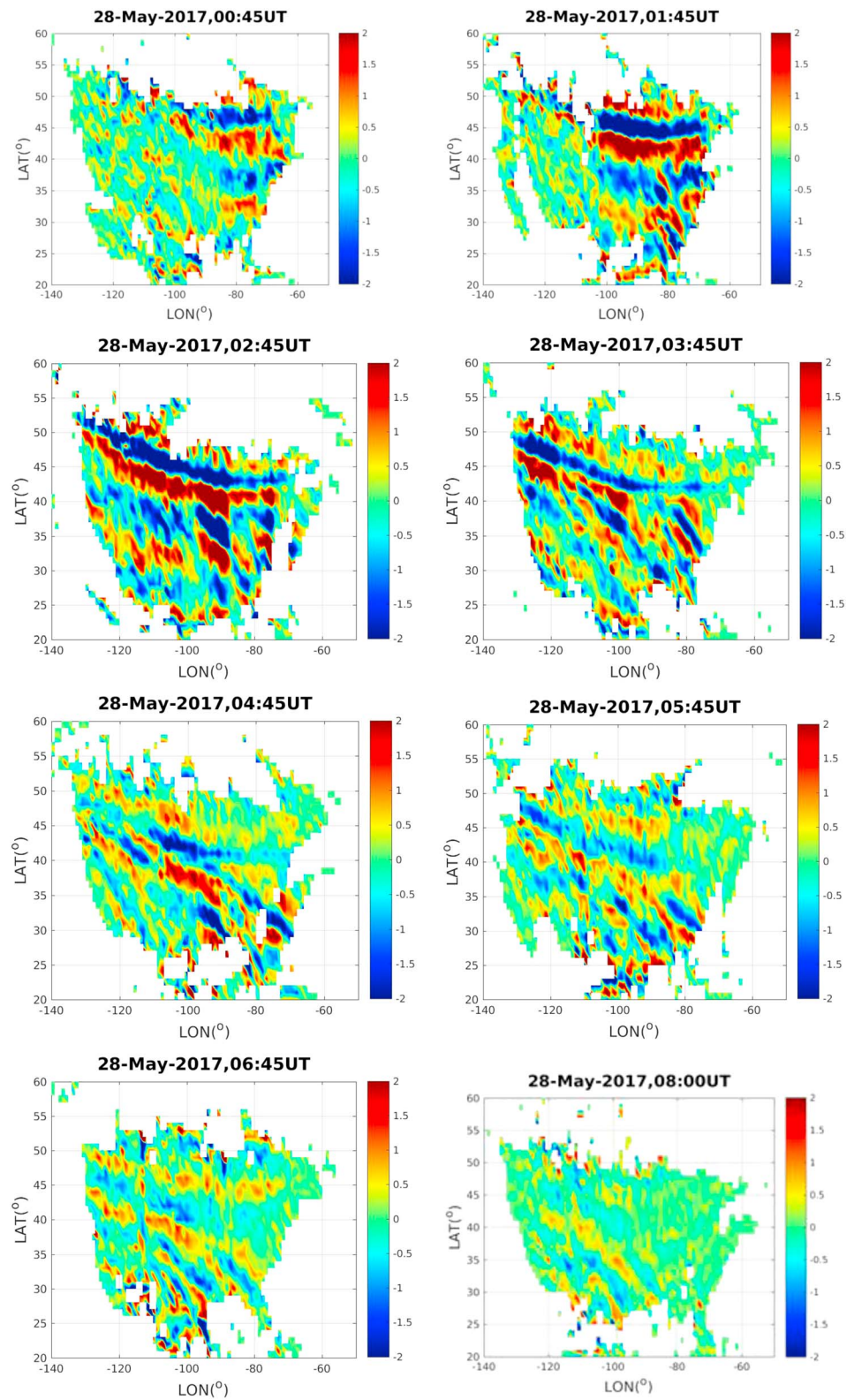
Figure 3. Two-dimensional maps of traveling ionospheric disturbances over North America at selected times during 0045 to 0800 UT (evening) during the main phase of the 2017 Memorial Day weekend geomagnetic storm.
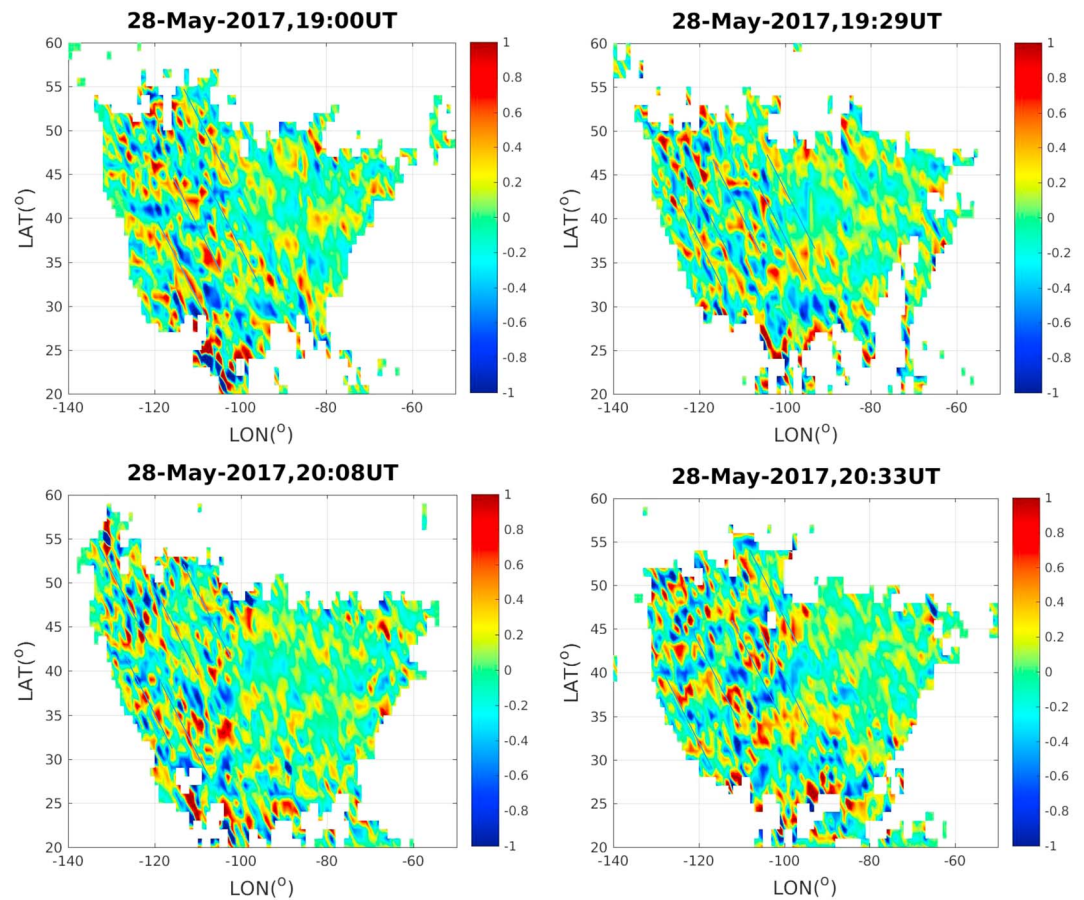
Figure 4. Two-dimensional maps of traveling ionospheric disturbances over North America at selected times during 1900 to 2033 UT (daytime) during the recovery phase of the 2017 Memorial Day weekend geomagnetic storm.

eastern standard time) as they traveled equatorward. (B) They are large in scale (i.e., LSTIDs), first appeared in the northeast, and subsequently traveled to the southwest region with a maximum velocity of 544 ± 70 m/s. (C) A second class of TID event was observed during the recovery phase of the storm. These TIDs were present during most of the rest of the day. Figure 4 shows selected 2-D TEC maps during TID activity from 1900 to 2033UT (i.e., 1200–1333 Pacific standard time). (D) The latter TIDs appeared with relatively weaker amplitudes and shorter wavelengths as compared to LSTIDs; hence, they can be classified as MSTIDs. (E) MSTIDs of this type propagated in a poleward-eastward direction with an average velocity of 192 ± 10 m/s.

To further analyze the properties of the observed TID waves (such as period, wavelength, and velocity), we constructed keogram plots in latitude and longitudes as a function of time, separating North America into three sections: the western (115°), central (100°), and eastern (80°) regions. Figures 5a–5c show these TEC perturbations as a function of latitude and time for the western central and eastern region, respectively. (F) In Figure 5a, note that TEC perturbations (LSTIDs) maximized around 0000–1200UT, substantially weakened during the rest of the day. (G) Both Figures 3 and 5 indicate that LSTIDs moved with a higher speed in the central region, near 100° longitude. (H) Figure 5 shows that besides the equatorward-propagating LSTIDs observed between 0045–0800UT (Figure 5a), a poleward-propagating and slower-speed MSTID clearly occurred around 1800–2100 UT (Figure 5d). These correlate well with the equatorward traveling wave of Figure 3 and the poleward traveling wave of Figure 4, respectively. Similar TEC perturbation features were observed in the central and eastern U.S. regions, as plotted in Figures 5b and 5c. Figures 5d and 5e show poleward propagating MSTIDs in the western and central regions, but with lower velocity compared to the LSTIDs ones. Figure 5f shows very weak MSTIDs, which implies that the poleward eastward MSTID movements have obviously dissipated before reaching the eastern side. This behavior can also be observed in the MSTID maps of Figures 6 and 7.
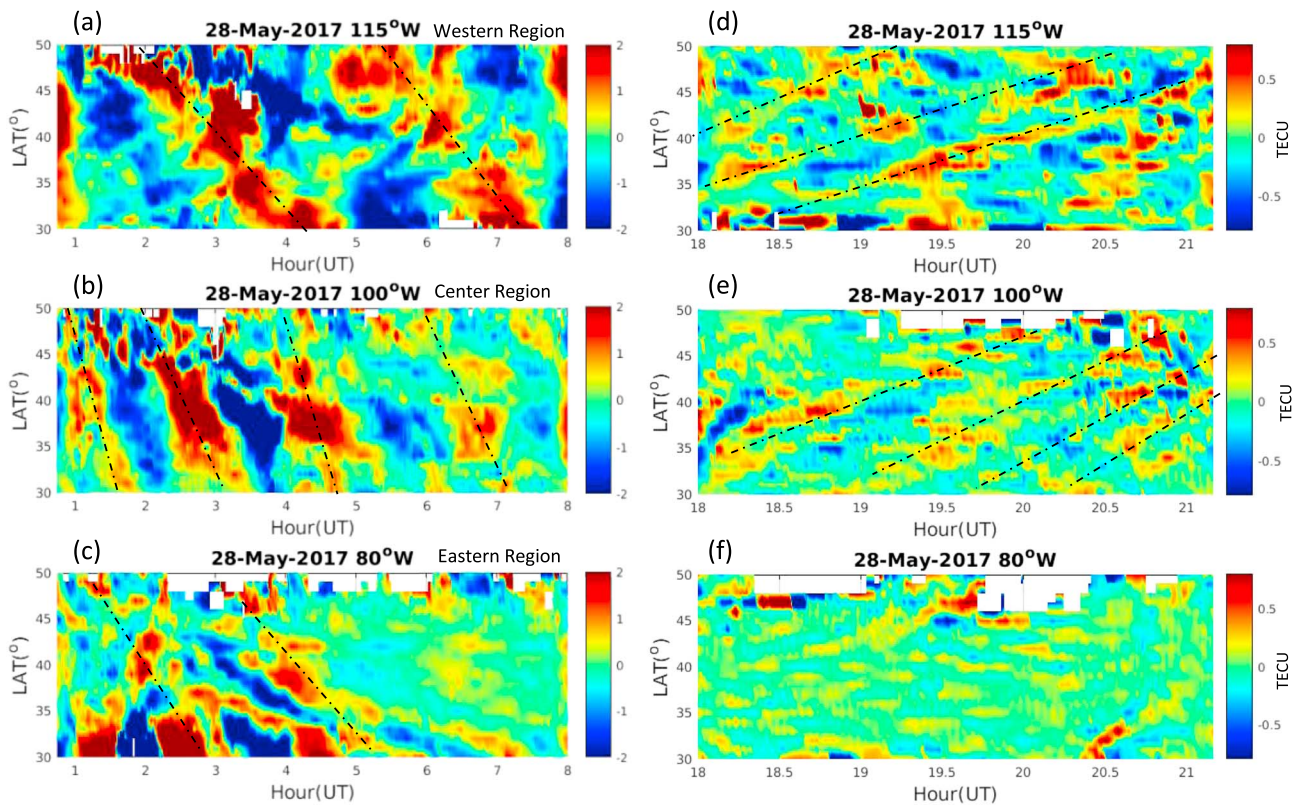
Figure 5. Keogram plot of total electron content perturbation on 28 May 2017 for equatorward large-scale traveling ionospheric disturbances during storm main phase and poleward medium-scale traveling ionospheric disturbances during storm recovery phase. (a–e) The longitudinal cuts of 115, 100, and 80°W equatorward and poleward, respectively.

3.3. Main Characteristics of Equatorward LSTIDs and Poleward MSTIDs

We computed the periodicity, velocity, and wavelength for TIDs in different regions. Figure 8 shows the resulting classification of TID wave features, comparing the equatorward (LSTIDs) and poleward (MSTIDs) features, which were quite different in different regions. (I) Figure 8 (top panel) indicates that in the western region, equatorward propagating LSTIDs traveled with a period of 2.00–2.30 hr, velocity of 268.67–308.33 m/s, and a wavelength of 2,220 ± 62 km. In the central region, the equatorward propagating LSTIDs have a period of 0.85–1.00 hr, and moved faster, with velocity of 462.50–544.12 m/s and a wavelength of 1,665 ± 70 km. Finally, in the eastern region, the equatorward propagating LSTIDs traveled with a period of 2.00 to 2.50 hr, velocity of 246.67–308.33 m/s, and wavelength of 2,220 ± 120 km. (J) Generally, the equatorward LSTIDs were aligned in NW-SE directions with ~5000 ± 454 km wavefront in the direction (i.e., from coast to coast). The variation in the LSTID velocity could be influenced by the different geomagnetic storm effects at different locations. According to Danilov and Lastovicka (2001), the effects of geomagnetic storm at different altitudes and latitudes differ in development, time, and intensity. Prolss (1995) also showed that response of the F region ionosphere seen at different ionospheric stations may be different during the same storm depending on the station's coordinates, local time of the geomagnetic storm onset, and some other parameters. More extensive discussion is given in the next section.

On the other hand, the poleward-MSTIDs have fundamentally different features, as indicated in Figure 8 (bottom panel). (K) Poleward propagating MSTIDs were characterized by a maximum period of 1.00 ± 0.04 hr, maximum velocity of 154 ± 25 m/s, and maximum wavelength of 55 ± 47 km in the western region. In the central region, MSTIDs traveled with a period of 1.00 ± 0.07 hr, velocity of 231 ± 8 m/s, and a wavelength of 832 ± 31 km. However, the MSTIDs are not well defined in the eastern region during this period of time (Figures 3, 6, and 7). The very weak/absent MSTIDs in the eastern region support the idea that the MSTIDs observed in both western and central regions (and propagating in the northeast direction) are seeded locally by convection induced gravity wave activity. Detail discussion can be found in section 4.2 of this study. (L)
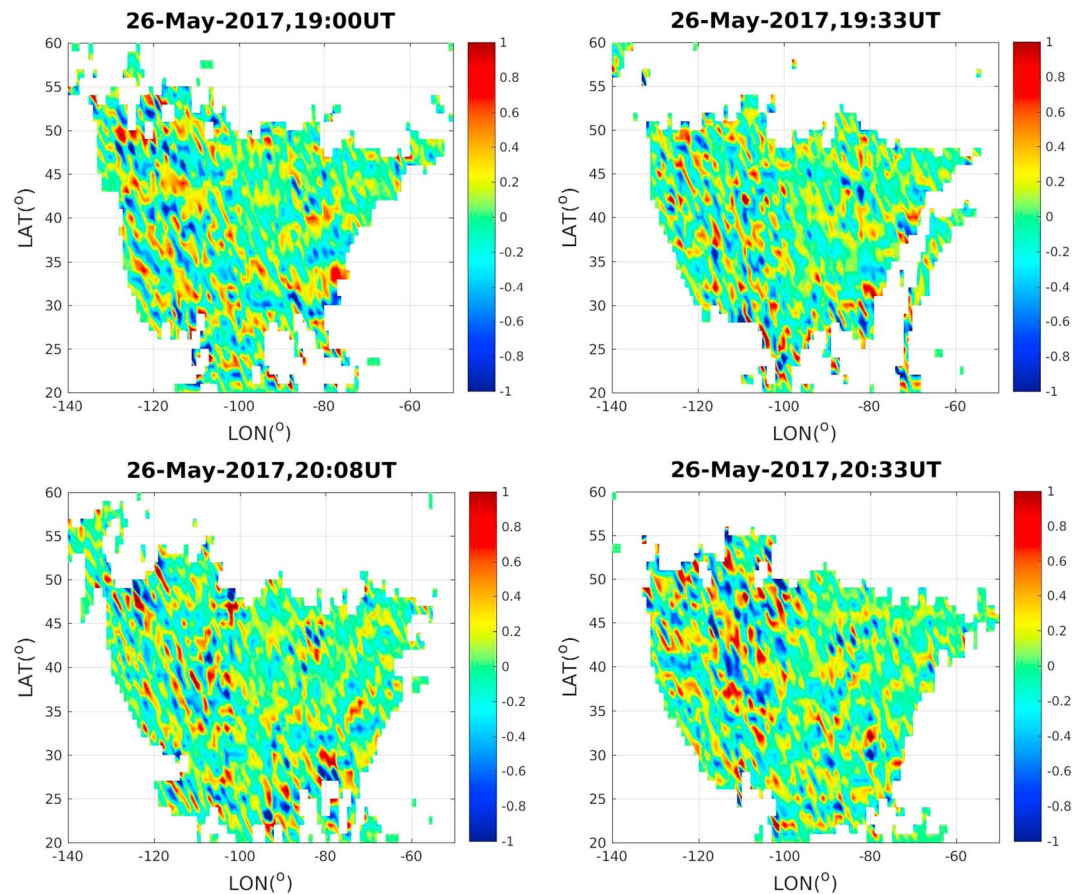
Figure 6. Two-dimensional maps of traveling ionospheric disturbances over North America at selected times during 2000 to 2130 UT (daytime) on 26 May 2017, a prestorm period.

Wavelengths of poleward propagating TIDs were aligned in the southeast-northwest (SE-NW) direction with ~832 ± 31 km horizontal wavelength.

4. Analysis and Discussion

4.1. Mechanisms Responsible for Equatorward TIDs

TID properties described by (A–B) and (H–J) clearly indicate the presence of a number of LSTIDs during the main phase of the Memorial Day weekend storm, and we discuss in this section probable mechanisms responsible for LSTID generation. Modeling work by Fuller-Rowell et al. (1996) has shown that the energy input in the auroral region can heat the thermosphere and drive equatorward wind surges, greatly contributing to the seeding of equatorward-traveling LSTIDs. Ding et al. (2007) used GPS-TEC data to detect LSTIDs linked to the westward auroral electrojet as detected through decreases in the H and X components of the magnetic field. Earlier studies, such as Chimonas and Hines (1969), have shown that geomagnetic disturbances have the ability to drive or trigger AGWs through the processes of Joule heating and Lorentz forcing. Tsugawa et al. (2004) carried out a statistical study of LSTIDs over Japan and showed that the occurrence rate of LSTIDs increased as Kp index values increased.

Based on these findings, we discuss here whether the Memorial Day weekend geomagnetic storm generated the LSTID observed during the storm's main phase. For this analysis, we used the Y component of magnetic field derived from the array of magnetometer measurements provided by the AUTUMN and AUTUMNX Virtual Magnetic Observatories and SuperMAG network. We first check for the location of the auroral oval by using the network of magnetometers over North America that are shown in Figure 1a with the blue star shapes. The top panel of Figure 9 shows maximum values of Y component obtained with 1-min resolution in latitudinal ranges 50–60° (blue), 60–70° (red), and 70–80° (green). It clearly shows that the largest impact of
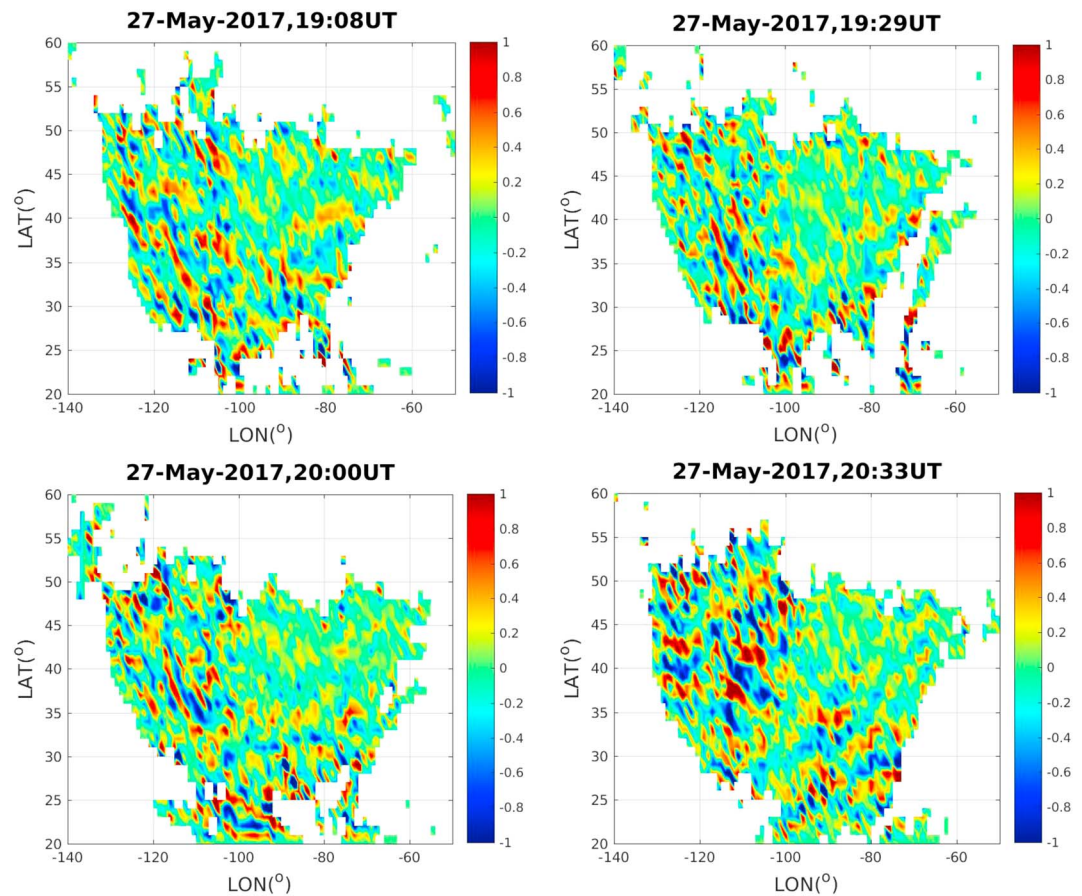
Figure 7. Two-dimensional maps of traveling ionospheric disturbances over North America at selected times during 2000 to 2130 UT (daytime) on 27 May 2017 during the main storm phase of the 2017 Memorial Day weekend storm.

the auroral energy source occurs mainly between latitudes 50 and 60°. We then used the locations of the magnetometers at 56.24°N, 120°W (western region); 55.15°N, 105.26°W (central region); and 60.20°N, 75.65°W (eastern region) as given by red circles in Figure 1a. These are strategic locations around the auroral electrojet over North America, corresponding well to the principal area of TID observations, and the magnetometers sampled the effective impact of the geomagnetic storm. Figures 9a–9c show temporal variations of magnetic field Y component observed by three magnetometers stationed at the western (FSJ), eastern (SALU), and central (LARG) regions, respectively. The blue curve represents a diurnal variation of magnetic activity during a day (26 May 2017) without geomagnetic storms; the red curve plots magnetic field activity on the Memorial Day weekend. Large fluctuations (increase and decrease) of up to 200 nT occurred at the FSJ and SALU stations at the onset of the main storm phase compared to the control day (26 May 2017), on which magnetometer perturbations remained near 0 nT. According to Hunsucker (1982), a decrease or increase in the X or Y component indicates an enhancement of the westward or eastward electric current, which may subsequently intensify the rate of charged particles' transfer of momentum from ions/electrons to neutrals through collisions. This mechanism can induce AGWs, which can seed LSTIDs through the Lorentz force ($\mathbf{J} \times \mathbf{B}$) or Joule heating ($\mathbf{J} \times \mathbf{E}$). The most obvious magnetometer feature is the very intense fluctuations at the LARG station shown in Figure 9c. The value of decrease of the Y component during the main phase of the storm exceeded $-1,000$ nT. Looking closely at the Figure 9c, three intermittent peaks in LARG perturbations occurred at 00.67UT, 01.70UT, and 02.50UT (as indicated by the light shaded box). As the peak amplitude spikes increase, we observed a corresponding simultaneous increase in the generation and peak amplitude of the LSTIDs, as shown in Figure 3. The third magnetometer peak at 02.50UT (indicated by the blue arrow) also correlates well with the peak of the LSTIDs (i.e., a period of well-developed LSTIDs) also at ~02.50UT (Figure 3), suggesting a nearly one-to-one response of the ionosphere to the auroral energy source. Hence, this finding suggests that the observed growth in the LSTID was interconnected with this intermittent
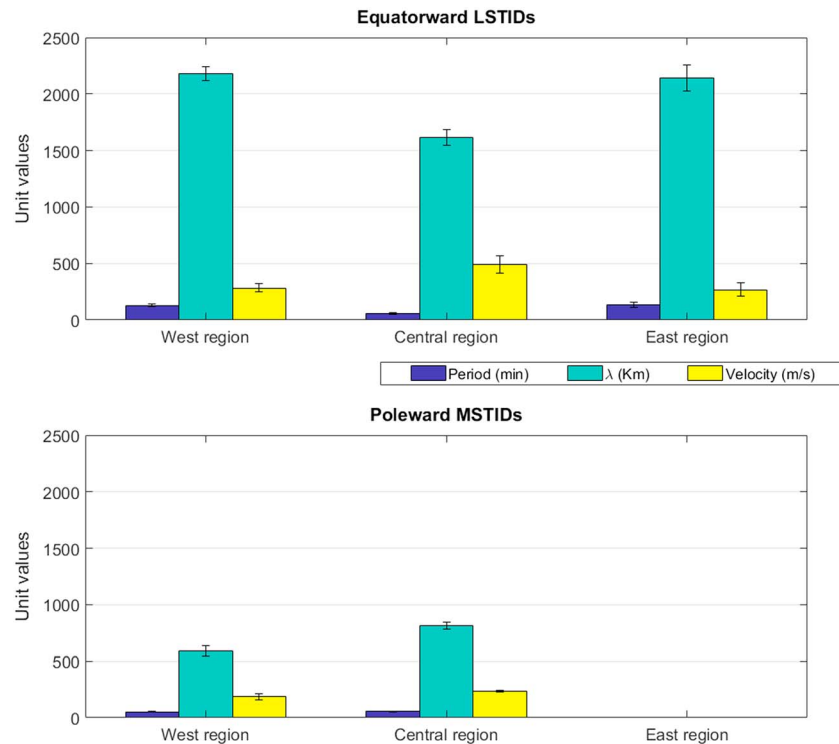
Figure 8. The top panels represent the equatorward large-scale traveling ionospheric disturbances features, and the bottom panel represents poleward medium-scale traveling ionospheric disturbance features. The error bars indicate the uncertainty of the waves.

energy input from the auroral source into the ionospheric system in a clear indication of magnetosphere-ionosphere coupling. The maximum energy input represented by the blue curve in the top panel of Figure 9 is located within 50 to 60° latitudes, which is very close to the onset of the LSTID observation around 50 to 53° latitude. Hence, there is no significant propagation time between the observed source and the onset of the LSTIDs. Habarulema et al. (2016) have also shown this kind of simultaneous correlation between the peak of H component of magnetometers and that of LSTIDs over the American sector, and they associated this behavior to penetration electric resulting from the southward turning of IMF during the geomagnetic storm. Another interesting observation is characteristic (G), indicating that the fastest-moving LSTIDs are observed in the central region, as shown in Figures 3 and 5. This observation correlates well with the highest peak of magnetic variation observed at the LARG magnetometer station. It is possible to note that the faster moving TIDs in the central region are closer to the disturbance source region in the aurora zone as shown by the magnetometer data in Figure 9. We employed the wavelet power spectra analysis of magnetometer fluctuations to check the periodicity of the magnetic activity, and results are plotted on the right-hand side of Figure 9. The black line represents confidence limit. We found consistent periods of 0.25, 0.50, and 1 to 3 hr in all Y components at different stations, which are homologous to the periods observed in both polewar and equatorward TIDs, as discussed earlier. Finally, it is also noted that magnetic declination (Figure 1a) around 115° longitude (western region), 100° longitude (central region), and 80° longitude (eastern region) are ~15, ~0, and ~ −15, respectively. The combined declination and zonal wind effects are known to produce ionospheric longitudinal differences (Zhang et al., 2011). Similarly, the different magnetic field declination values across continental United States could cause different damping effects on the meridional propagation of the ion disturbances at different longitudes. Further verification of this behavior will be carried out in future studies.

4.2. Mechanism Responsible for Poleward TID Propagation

Poleward MSTID waves are established from wave properties mentioned at C–F and K–L. The poleward propagating TIDs of 28 May 2017 (geomagnetic disturbed day) shown in Figure 4 cannot be
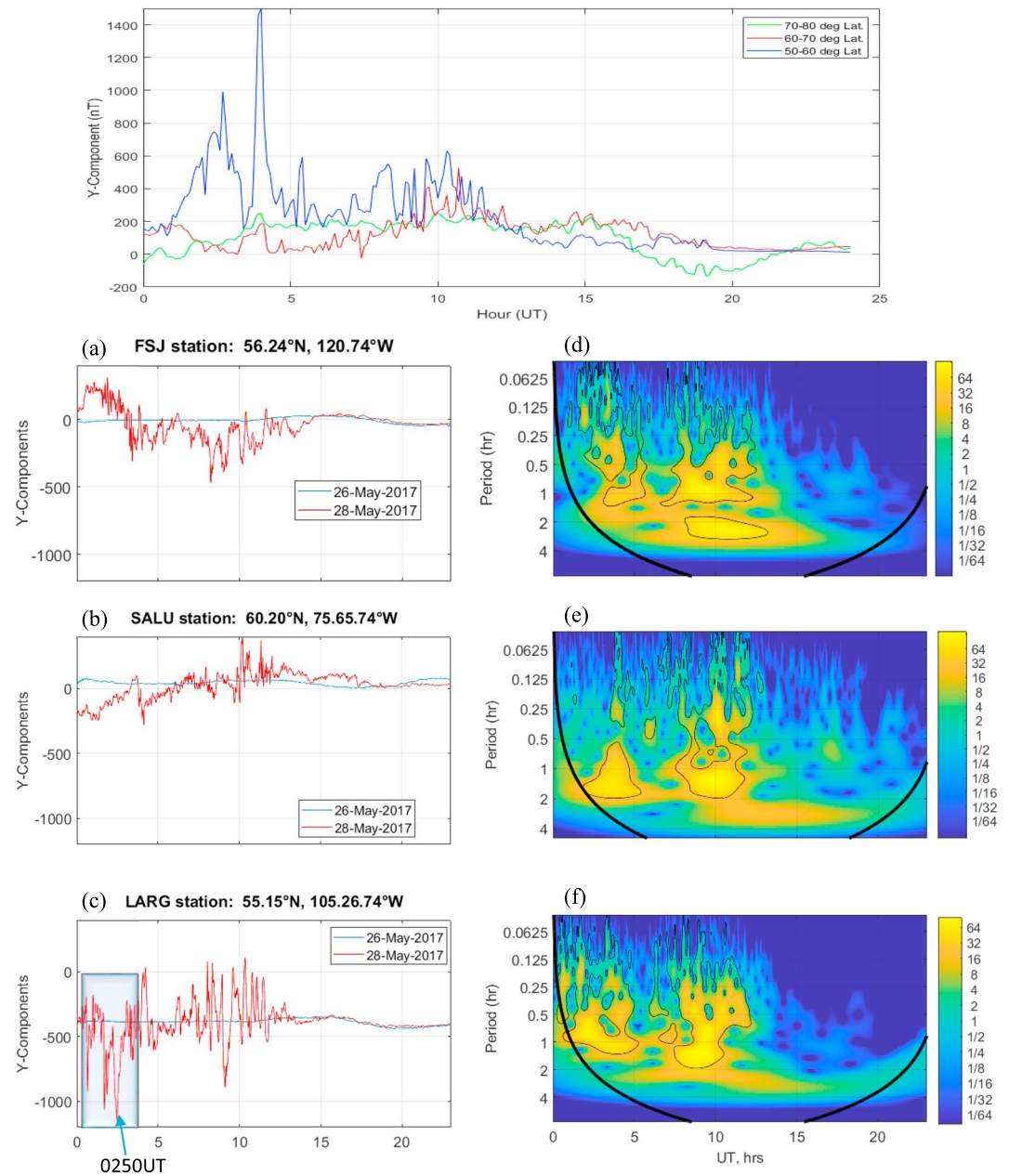
Figure 9. Top panel show the maximum values of magnetic east-component during the 28 May 2017 from different magnetometer distribution over 50–60° lat (blue color), 60–70° lat (red color), and 70–80° lat (green color). (a–c) Particular magnetometer stations during the 2017 Memorial Day weekend storm on 28 May (red curve; storm main phase) and 26 May (blue curve; prestorm). (d and e) Spectral wavelet analysis for each corresponding magnetometer station on storm day 28 May.

associated with the storm activity, since similar poleward TIDs were also observed on geomagnetically quiet days. Figures 6 and 7 provide two examples of quiet time poleward MSTID structures similar to Figure 4, but for 26 and 27 May 2017. This finding implies that poleward MSTIDs observed on 28 May during the main storm phase are not driven by processes related to the geomagnetic storm, since the same poleward MSTIDs with similar properties were observed during nongeomagnetic storm days.
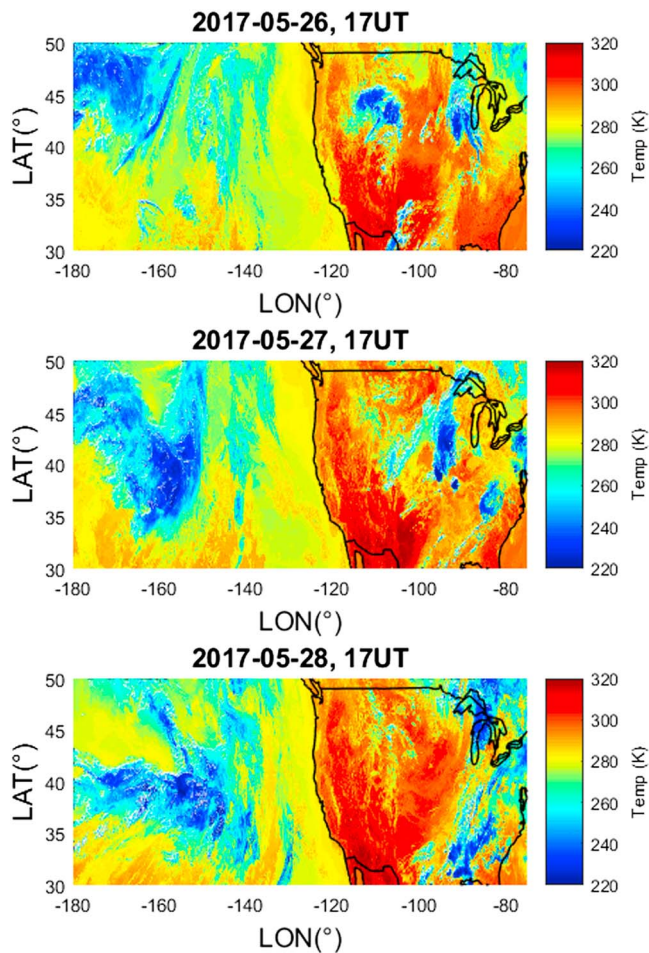
Figure 10. Observation of deep clouds in brightness temperature from GOES satellite on 26–28 May 2017 in panels a–c, respectively.

In the section, we further investigated other nongeomagnetic TID sources. Many studies have proposed that significant AGW/TIDs can be generated from upward propagating meteorological processes (e.g., orography and cloud convection activities in the troposphere and stratosphere), motions of the ground during earthquakes, and tsunamic events. To our knowledge, there were neither significant natural disasters nor man-made explosions during 26–30 May 2017 over North America. Hence, we focus here on whether lower atmosphere regions associated with cloud convection activity provided the main source for AGW/TIDs. Using model simulation studies, Vadas and Fritts (2006), Medvedev et al. (2011), and Yigit et al. (2012) have demonstrated that convectively generated gravity waves can propagate from the lower atmosphere into the thermosphere-ionosphere system. In addition, many authors have used experimental studies to show the ionospheric responses to tropospheric events (de Paula et al., 2015; Goncharenko & Zhang, 2008; Jonah et al., 2014; Paes et al., 2014). For example, the studies by Vadas and Liu (2009), Azeem et al. (2015), and Jonah et al. (2016) used tropospheric convective plumes perturbation sources to show a global and regional GW associated perturbation in TEC. Nakamura et al. (2003) and Shume et al. (2014) also used tropospheric convective plumes perturbations source to show connections between usual periodicity in the intensity of EEJ current and the preferred propagation direction of GW in an all-sky imager during all seasons of the year. These and other related studies clearly demonstrate the importance of troposphere-ionosphere coupling through convection activity as an important factor of AGW/TID seeding in the ionosphere.

Hence, in the present study, we investigated the poleward propagating MSTIDs on 26–28 May 2017 over the western region of the United States by using the BT data from the GOES satellite as provided by the NASA GES DISC. We found deep convection activities on almost a daily basis at the U.S. west coast, over the Pacific Ocean. Figure 10 shows hourly resolution of BT at 20UT for 26–28 May. According to Hoffmann, and Alexander (2010), BT < 250 K corresponds to deep/strong convection cases and BT around the Pacific Ocean was well below 250 K on all 3 days. The deep convection activity shown in Figure 10 is during the similar time periods and in locations adjacent to where the poleward TIDs were observed. This evidence suggests that poleward TIDs could have resulted from a convective-induced AGW. We verified AGW activity levels on 26–28 May 2017 by using observations from SABER, on board NASA's TIMED satellite. Figure 10 shows the signature of AGWs as determined from SABER differential temperature profiles. The SABER measurements used data collected within 25° to 50° latitudes and −120° to −140° longitudes for the ascending phase. We focus our investigation on altitude between 60 to 100 km in order to explore the activity of gravity waves, their survival to the thermosphere, consequent initialization of secondary AGW and generation of instability. The pink solid curve in Figure 11 (top panels) shows the temperature profile (K); the blue curves plot a polynomial filtered curve (order = 10) that is used as a detrended line to yield a smooth background temperature profile (T_{mean}). The bottom panels show the vertical wavelength of the gravity waves. This is determined by taking the fast Fourier transform of the different temperature derived above and using the equation $\lambda \approx 2\pi/k$ for the determination of the wavelength (λ), where k is the wave number.

The change in temperature with increasing altitude can be used to show gravity wave signature with downward phase and upward energy propagation (Hines, 1960). We observed larger dynamic variations at altitudes between 75 and 100 km (see Figure 11, top panels). Hence, the region of interest for the present study is between 60- and ~100-km altitude. We are interested in whether the gravity wave found around this region can propagate up to the F region ionosphere. At these altitudes, AGWs are affected by a number of factors, such as energy loss through viscosity, nonlinear effects in cases where the
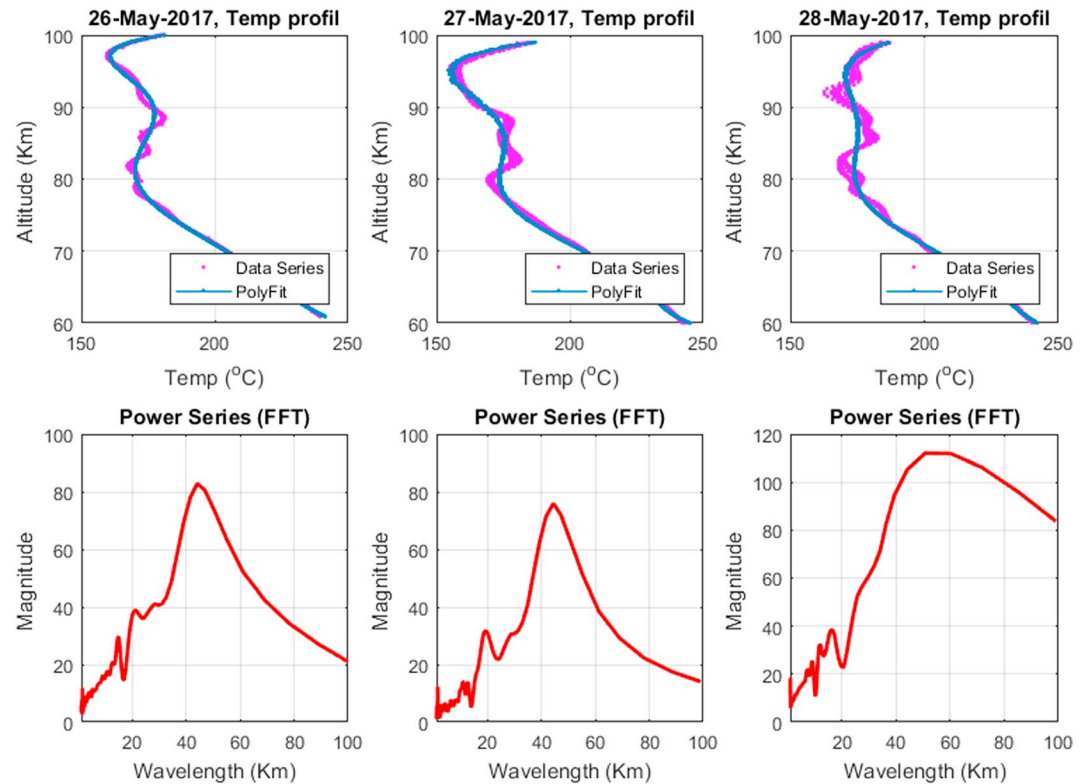
Figure 11. Top panel: atmospheric temperature profile from the Thermosphere-Ionosphere-Mesosphere Energetics and Dynamics Sounding of the Atmosphere using Broadband Emission Radiometry (TIMED SABER) instrument satellite (pink color) with polynomial fit (blue color). Bottom panel: the peak of the wavelength obtained by taken the fast Fourier transform analysis of the differential temperature. The left to right columns show observations for 26–28 May 2017, respectively, and data are taken from 25 to 50° latitude and −120° to −140° longitude for the satellite ascending phase.

wave amplitude becomes too large at higher altitudes, attenuation or ducting due to changes in atmospheric properties, and the Earth's curvature, winds, and tides. However, when AGWs survive these damping mechanisms, they could become larger in scale (referred to as secondary gravity waves) due to large horizontal gradients in the thermosphere-ionosphere system and can subsequently propagate globally, as shown by Vadas and Liu (2009). In the present study we observe vertical wavelength of 40 to 55 km as shown by Figure 11 bottom panels. The wavelength of the gravity wave is an important parameter of determining how far the gravity wave travels through the atmosphere. The wave breaking systems (some of which are mentioned above) referred to as thermospheric body force are mechanisms capable of generating secondary gravity waves. According to Vadas (2007), the gravity waves most important for thermospheric body force have vertical wavelength of ~50 to 65 km. In the present study we observe wavelength between 40 and 55 km from the convection induced gravity wave, as shown by Figure 11 (bottom panels). Therefore, it is possible that these gravity waves observed in this study caused secondary gravity waves (through the mechanism explained above), which survive to the *F* region and generate the observed poleward MSTIDs.

There is clear evidence during 26–28 May 2017 of deep atmospheric convection in the coastal Pacific Ocean region (in the region of 25° to 50° latitudes and −120° to −180° longitudes), close to the continental United States, as shown by GOES satellite images in Figure 10, and AGW signatures in SABER temperature data at region of 25° to 50° latitudes and −120° to −140° longitudes, which is closer the United States western region of California, as shown in Figure 11. We therefore suggest that AGWs generated from tropospheric weather convection sources can propagate into higher altitudes and penetrate deep into the upper atmosphere, where they manifest as TIDs. We also associate the existence of poleward propagating MSTIDs, subsequently observed partly during the recovery phase of the Memorial Day weekend geomagnetic storm and ubiquitously during geomagnetically quiet days, with the convection-induced AGW source. We also note that as

these MSTIDs were observed in the extended range of longitudes, we cannot rule out gravity wave generation related to steep orographic gradients around Rocky Mountains or Sierra Nevada. However, separation of relative roles of different meteorological sources of gravity waves is beyond the scope of this study and can be addressed in a separate effort.

5. Conclusions

Using the GNSS receivers widely distributed over United States, networks of magnetometers over North America, and satellite measurements from the NOAA-GOES and SABER missions, we investigated the TID characteristics during the 28 May 2017 Memorial Day weekend geomagnetic storm and other quiet geomagnetic periods. We report equatorward LSTID owning to the 2017 Memorial Day weekend geomagnetic storm and poleward MSTID propagation owning to atmospheric convection activity over the Pacific Ocean. Hence, this study reveals the coupling of magnetosphere and ionosphere system as well as the interaction between the lower and upper atmosphere. The main conclusions are listed here:

Large-scale and equatorward-propagating TIDs were generated from periodic energy input from the auroral source as a result of the 2017 Memorial Day weekend storm. The LSTID lasted for the whole period of the main phase of the storm.

The TID velocity changes from one region to another. We observed that TIDs move faster at the central region. This behavior is attributed to the higher source of auroral energy, and the difference in the magnetic field declination at different region is suggested to be the cause of this wave behavior.

Based on our results shown in Figures 10 and 11, we suggest that the deep convection-induced AGWs play significant role in the poleward propagating MSTIDs during geomagnetically quiet days (26–27 May 2017) and during the recovery phase of the storm (28 May 2017). AGW from Rocky Mountain and/or Sierra Nevada waves could also contribute significantly to the observed MSTIDs.

References

Azeem, I., Yue, J., Hoffmann, L., Miller, S. D., Straka, W. C., & Crowley, G. (2015). Multisensor profiling of a concentric gravity wave event propagating from the troposphere to the ionosphere. *Geophysical Research Letters*, *42*, 7874–7880. https://doi.org/10.1002/2015GL065903

Chimonas, G., & Hines, C. O. (1969). Atmospheric gravity waves launched by auroral currents. *Planetary and Space Science*, *18*(4), 565–582. https://doi.org/10.1016/0032-0633(70)90132-7

Coster, A. J., Goncharenko, L., Zhang, S., Erickson, P. J., Rideout, W., & Vierinen, J. (2017). GNSS observations of ionospheric variations during the 21 August 2017 solar eclipse. *Geophysical Research Letters*, *17*, 349–352. https://doi.org/10.1002/2017GL075774

Danilov, A. D., & Lastovicka, J. (2001). Effects of geomagnetic storms on the ionosphere and atmosphere. *International Journal of Geomagnetism and Aeronomy*, *2*(3), 209–224.

de Paula, E. R., Jonah, O. F., Moraes, A. O., Kherani, E. A., Fejer, B. G., Abdu, M. A., et al. (2015). Low-latitude scintillation weakening during sudden stratospheric warming events. *Journal of Geophysical Research: Space Physics*, *120*, 2212–2221. https://doi.org/10.1002/2014JA020731

Ding, F., Wan, W., Ning, B., & Wang, M. (2007). Lager-scale traveling ionospheric disturbances observed by GPS total electron content during the magnetic storm of 29–30 October 2003. *Journal of Geophysical Research*, *112*, A06309. https://doi.org/10.1029/2006JA012013

Ding, F., Wan, W., Ning, B., Zhao, B., Li, Q., Wang, Y., et al. (2013). Observations of poleward-propagating large-scale traveling ionospheric disturbances in southern China. *Annales de Geophysique*, *31*, 377–385. https://doi.org/10.5194/angeo-31-377

Duly, T. M., Huba, J. D., & Makela, J. J. (2014). Self-consistent generation of medium-scale traveling ionospheric disturbances (MSTIDs) within the SAMI3 numerical model. *Journal of Geophysical Research: Space Physics*, *119*, 6745–6757. https://doi.org/10.1002/2014JA020146

Fuller-Rowell, T. J., Codrescu, M. V., Mo•ett, R. J., & Quegan, S. (1996). On the seasonal response of the thermosphere and ionosphere to geomagnetic storms. *Journal of Geophysical Research*, *101*, 2343–2353.

Goncharenko, L., & Zhang, S. R. (2008). Ionospheric signatures of sudden stratospheric warming: Ion temperature at middle latitude. *Geophysical Research Letters*, *35*, L21103. https://doi.org/10.1029/2008GL035684

Habarulema, J. B., Katamzi, Z. T., & Yizengaw, E. (2015). First observations of poleward large-scale traveling ionospheric disturbances over the African sector during geomagnetic storm conditions. *Journal of Geophysical Research: Space Physics*, *120*, 6914–6929. https://doi.org/10.1002/2015JA021066

Habarulema, J. B., Katamzi, Z. T., Yizengaw, E., Yamazaki, Y., & Seemala, G. (2016). Simultaneous storm time equatorward and poleward large-scale TIDs on a global scale. *Geophysical Research Letters*, *43*, 6678–6686. https://doi.org/10.1002/2016GL069740

Hernandez-Pajares, M., Juan, J. M., & Sanz, J. (2006). Medium-scale traveling ionospheric disturbances affecting GPS measurements: Spatial and temporal analysis. *Journal of Geophysical Research*, *111*, A07S11. https://doi.org/10.1029/2005JA011474

Hines, C. O. (1960). Internal atmospheric gravity waves at ionospheric heights. *Canadian Journal of Physics*, *38*(11), 1441–1481. https://doi.org/10.1139/p60-150

Hocke, K., & Schlegel, K. A. (1996). Review of atmospheric gravity waves and travelling ionospheric disturbances: 1982–1995. *Annales de Geophysique*, *14*(9), 917–940. https://doi.org/10.1007/s00585-996-0917-6

Hoffmann, L., & Alexander, M. J. (2010). Occurrence frequency of convective gravity waves during the North American thunderstorm season. *Journal of Geophysical Research*, *115*, D20111. https://doi.org/10.1029/2010JD014401

Horinouchi, T., Nakamura, T., & Kosaka, J. I. (2002). Convectively generated mesoscale gravity waves simulated throughout the middle atmosphere. *Geophysical Research Letters*, *29*(21), 2007. https://doi.org/10.1029/2002GL016069

Horvath, I., & Lovell, B. C. (2010). Large-scale traveling ionospheric disturbances impacting equatorial ionization anomaly development in the local morning hours of the Halloween Superstorms on 29–30 October 2003. *Journal of Geophysical Research*, *115*, A04302. https://doi.org/10.1029/2009JA014922

Huba, J. D., Drob, D. P., Wu, T. W., & Makela, J. J. (2015). Modeling the ionospheric impact of tsunami-driven gravity waves with SAMI3: Conjugate effects. *Geophysical Research Letters*, *42*, 5719–5726. https://doi.org/10.1002/2015GL064871

Hunsucker, R. D. (1982). Atmospheric gravity waves generated in the high latitude ionosphere: A review. *Reviews of Geophysics and Space Physics*, *20*(2), 293–315. https://doi.org/10.1029/RG020i002p00293

Janowiak, J. E, Joyce, R. J., & Xie, P. (2017). NCEP/CPC L3 half hourly 4 km global (60°S–60°N) merged IR V1, Greenbelt, MD, Goddard Earth Sciences Data and Information Services Central (GES DISC), Accessed [Data Access Date] 10.5067/P4HZB9N27EKU.

Jonah, O. F. (2017). A study of daytime MSTIDS over equatorial and low latitude regions during tropospheric convection: observations and simulations, Doctoral *thesis of the Graduate Course in Space Geophysics*, http://urlib.net/sid.inpe.br/mtc-m21b/2017/02.02.15.30

Jonah, O. F., de Paula, E. R., Kherani, E. A., Dutra, S. L. G., & Paes, R. R. (2014). Atmospheric and ionospheric response to stratospheric sudden warming of January 2013. *Journal of Geophysical Research: Space Physics*, *119*, 4973–4980. https://doi.org/10.1002/2013JA019491

Jonah, O. F., Kherani, E. A., & de Paula, E. R. (2016). Observation of TEC perturbation associated with medium-scale traveling ionospheric disturbance and possible seeding mechanism of atmospheric gravity wave at a Brazilian sector. *Journal of Geophysical Research: Space Physics*, *121*, 2531–2546. https://doi.org/10.1002/2015JA022273

Jonah, O. F., Kherani, E. A., & De Paula, E. R. (2017). Investigations of conjugate MSTIDS over the Brazilian sector during daytime. *Journal of Geophysical Research: Space Physics*, *122*, 9576–9587. https://doi.org/10.1002/2017JA024365

Kherani, E. A., Lognonné, P., Hébert, H., Rolland, L., Astafyeva, E., Occhipinti, G., et al. (2012). Modelling of the total electronic content and magnetic field anomalies generated by the 2011 Tohoku-Oki tsunami and associated acoustic-gravity waves. *Geophysical Journal International*, *191*, 1049–1066. https://doi.org/10.1111/j.1365-246X.2012.05617.x

Kotake, N., Otsuka, Y., Tsugawa, T., Ogawa, T., & Saito, A. (2007). A. Statistical study of medium-scale traveling ionospheric disturbances observed with the GPS networks in Southern California. *Earth, Planets and Space*, *59*(2), 95–102. https://doi.org/10.1186/BF03352681

MacDougall, J., Abdu, M., Batista, I., Fagundes, P. R., Sahai, Y., & Jayachandran, P. T. (2009). On the production of traveling ionospheric disturbances by atmospheric gravity waves. *Journal of Atmospheric and Solar - Terrestrial Physics*, *71*(17-18), 2013–2016. https://doi.org/10.1016/j.jastp.2009.09.006

Medvedev, A. S., Yigit, E., Hartogh, P., & Becker, E. (2011). Influence of gravity waves on the Martian atmosphere: General circulation modeling. *Journal of Geophysical Research*, *116*, E10004. https://doi.org/10.1029/2011JE003848

Nakamura, T., Aono, T., Tsuda, T., Admiranto, A. G., Achmad, E., & Suranto (2003). Mesospheric gravity waves over a tropical convective region observed by OH airglow imaging in Indonesia. *Geophysical Research Letters*, *30*(17), 1882. https://doi.org/10.1029/2003GL017619

Oliver, W. L., Otsuka, Y., Sato, M., Takami, T., & Fukao, S. (1997). A climatology of F region gravity wave propagation over the middle and upper atmosphere radar. *Journal of Geophysical Research*, *102*, 14,499–14,512.

Otsuka, Y., Kotake, N., Shiokawa, K., Ogawa, T., Tsugawa, T., & Saito, A. (2011). A. Statistical study of medium-scale traveling ionospheric disturbances observed with a GPS receiver network in Japan. In *Aeronomy of the Earth's atmosphere and ionosphere*, *IAGA Special Sopron Book Series*, (Vol. 2, pp. 291–299). https://doi.org/10.1007/978-94-007-0326-121

Otsuka, Y., Suzuki, K., Nakagawa, S., Nishioka, M., Shiokawa, K., & Tsugawa, T. (2013). GPS observations of medium-scale traveling ionospheric disturbances over Europe. *Annales de Geophysique*, *31*(2), 163–172. https://doi.org/10.5194/angeo-31-163

Paes, R. R., Batista, I. S., Candido, C. M. N., Jonah, O. F., & Santos, P. C. P. (2014). Equatorial ionization anomaly variability over the Brazilian region during boreal sudden stratospheric warming events. *Journal of Geophysical Research: Space Physics*, *119*, 7649–7664. https://doi.org/10.1002/2014JA019968

Prolss, G. (1995). In H. Volland (Ed.), *Ionospheric F-region storms, in Handbook of atmospheric electrodynamics*, (Vol. 2, pp. 195–248). Boca Raton: CRC *Press*.

Richmond, A. D. (1978). Gravity wave generation, propagation, and dissipation in the thermosphere. *Journal of Geophysical Research*, *83*(A9), 4131–4145. https://doi.org/10.1029/JA083iA09p04131

Rideout, W., & Coster, A. (2006). Automated GPS processing for global total electron content data. *GPS Solutions*, *10*(3), 219–228. https://doi.org/10.1007/s10291-006-0029-5

Saito, A., Nischimura, M., Yamamoto, M., Fukao, S., Tsugawa, T., Otsuka, Y., et al. (2002). Observations of traveling ionospheric disturbances and 3-m scale irregularities in the nighttime F-region ionosphere with the MU radar and a GPS network. *Earth, Planets and Space*, *54*(1), 31–44. https://doi.org/10.1186/BF03352419

Saito, S., Yamamoto, M., Hashiguchi, H., Maegawa, A., & Saito, A. (2007). Observational evidence of coupling between quasi-periodic echoes and medium scale traveling ionospheric disturbances. *Annales Geophysicae*, *25*, 2185–2194.

Shume, E. B., Rodrigues, F. S., Mannucci, A. J., & de Paula, E. R. (2014). Modulation of equatorial electrojet irregularities by atmospheric gravity waves. *Journal of Geophysical Research: Space Physics*, *119*, 366–374. https://doi.org/10.1002/2013ja019300

Song, Q., Ding, F., Wan, W., Ning, B., Liu, L., Zhao, B., et al. (2013). Statistical study of large-scale traveling ionospheric disturbances generated by the solar terminator over China. *Journal of Geophysical Research: Space Physics*, *118*, 4583–4593. https://doi.org/10.1002/jgra.50423

Tsugawa, T., Saito, A., & Otsuka, Y. (2004). A statistical study of large-scale travelling ionospheric disturbances using the GPS network in Japan. *Journal of Geophysical Research*, *109*, A06302. https://doi.org/10.1029/2003JA010302

Tsugawa, T., Otsuka, Y., Coster, A. J., & Saito, A. (2007). Medium-scale traveling ionospheric disturbances detected with dense and wide TEC maps over North America. *Geophysical Research Letters*, *34*, L22101. https://doi.org/10.1029/2007GL031663

Tsugawa, T., Saito, A., Otsuka, Y., & Yamamoto, M. (2003). Damping of large-scale traveling ionospheric disturbances detected with GPS networks during the geomagnetic storm. *Journal of Geophysical Research*, *108*(A3), 1127. https://doi.org/10.1029/2002JA009433

Vadas, S. L. (2007). Horizontal and vertical propagation and dissipation of gravity waves in the thermosphere from lower atmospheric and thermospheric sources. *Journal of Geophysical Research*, *112*, A06305. https://doi.org/10.1029/2006JA011845

Vadas, S. L., & Fritts, D. (2006). Influence of solar variability on gravity wave structure and dissipation in the thermosphere from tropospheric convection. *Journal of Geophysical Research*, *111*, A10S12. https://doi.org/10.1029/2005JA011510

Vadas, S. L. J., & Liu, A. (2009). Generation of large-scale gravity waves and neutral winds in the thermosphere from the dissipation of convectively generated gravity waves. *Journal of Geophysical Research*, *114*, A10310. https://doi.org/10.1029/2009JA014108

Vierinen, J., Coster, A. J., Rideout, W. C., Erickson, P. J., & Norberg, J. (2016). Statistical framework for estimating GNSS bias. *Atmospheric Measurement Techniques*, *9*(3), 1303 https://doi.org/10.5194/amt-9-1303-2016–1312.

Yigit, E., Medvedev, A. S., Aylward, A. D., Ridley, A. J., Harris, M. J., Moldwin, M. B., & Hartogh, P. (2012). Dynamical effects of internal gravity waves in the equinoctial thermosphere. *Journal of Atmospheric and Solar-Terrestrial Physics*, *90-91*, 104–116. https://doi.org/10.1016/j.jastp.2011.11.014

Zhang, S., Erickson, P. J., Goncharenko, L., Coster, A. J., Rideout, W., & Vierinen, J. (2017). Ionospheric bow waves and perturbations induced by the 21 august 2017 solar eclipse. *Geophysical Research Letters*, *44*, 12,067–12,073. https://doi.org/10.1002/2017GL076054

Zhang, S., Foster, R. J. C., Coster, A. J., & Erickson, P. J. (2011). East-west coast differences in total electron content over continental US. *Geophysical Research Letters*, *38*, L19101. https://doi.org/10.1029/2011GL049116